COMPUTATIONALLY EFFICIENT METHODOLOGY TO COMPUTE VIRTUAL PERMEABILITY OF FIBROUS LAMINATES

Biltu Mahato*, Stepan V. Lomov, Sergey G. Abaimov
Skolkovo Institute of Science and Technology, Bolshoy Boulevard 30, bld. 1, Moscow, Russia 121205
*corresponding author (biltu.mahato@skoltech.ru)

Keywords: X-ray computed tomography, CFD simulations, Virtual permeability, Cell approach

ABSTRACT

Production of composite structures by liquid composite molding is preceded by numerical modeling of the impregnation process to predict various parameters based on the permeability of reinforcement as the key input parameter. X-ray computed tomography (XCT) combined with computer simulations is a very effective and flexible technique for characterization of material permeability virtually. Although the XCT based virtual permeability method is robust, but it is limited by computation power hence restricted to a comparatively small computational sample which could be non-representative. In this research, an efficient methodology based on the cell approach to calculate virtual permeability of fibrous reinforcement based on micro XCT segmented images is presented and discussed. The 3D model was generated from the stack of XCT images, followed by the division of the model into several smaller domains, called cells, as consecutive and parallel (CaP) cells. The local permeability of each CaP cell was computed with the commercial computational fluid dynamics tool. The obtained permeability values were statistically processed considering each CaP cell, resulting in the global permeability value, and compared with the literature data and analytical predictions. The uniformity in the fiber distribution is assessed for each CaP cell and its effect on the local permeability is also discussed. A methodology for processing XCT segmented image of fiber reinforced composite laminate is assessed and successfully used to evaluate the uniformity of fiber distribution and its intra-tow virtual permeability.

ACRONYMS

3D	Three-dimensional
CaP	Consecutive and parallel
CFD	Computational fluid dynamics
FEM	Finite element method
GE model	Gebart-Endruweit model
IVPB	International Virtual Permeability Benchmark
LCM	Liquid composite molding
RTM	Resin transfer molding
VI	Vacuum infusion

1 INTRODUCTION

Liquid composite molding (LCM) process is widely used in the production of fiber-reinforced composite materials. In the LCM process, the dry fabric-reinforcement is placed in the pre-designed mold as per the design requirement, followed by impregnation of dry fabric with a thermoset polymer. The transfer and impregnation of thermoset polymer can be achieved by application of positive or negative operating pressure. For instance, in resin transfer molding (RTM), a positive operating pressure is used to push the thermoset polymer into the dry fabric-reinforcement. Whereas, in vacuum infusion (VI), a negative operating pressure is used to pull the thermoset polymer into the dry fabric-reinforcement. In the LCM process, it is crucial to impregnate the whole dry fabric-reinforcement without any dry spots in fastest possible time for economical reason. For such reason, the filling simulation is performed before the manufacturing to understand and measure the fill time, identify flow fronts, paths and possible dry spots, optimize the number, dimension, and placement of inlets and outlets, optimize impregnation pressure and monitor temperature rise as the thermoset is mixed with its hardener which could trigger the polymerization, followed by viscosity change [1]. The dry fabric-reinforcement has micro-channels; and simulation of thermoset polymer flow through such reinforcement is governed by Darcy's law given as,

$$v = -\frac{K\nabla P}{\mu} \tag{1}$$

Equation (1) can be further re-arranged to get the permeability as,

$$K = -\frac{\dot{m}\mu L}{\rho A \Delta P} \tag{2}$$

where v is the volume flow rate per unit area $[m/s]$, K is the permeability $[m^2]$, ∇P is pressure gradient $[Pa/m]$, μ is viscosity of fluid $[Pa.s]$, $\dot{m}$ is mass flow rate $[Kg/s]$, L is length $[m]$, A is cross sectional area $[m^2]$, and ΔP is pressure difference $[Pa]$.

The permeability of the fabric-reinforcement is an important parameter to simulate the thermoset polymer flow in the reinforcement. There are several methods to determine the permeability of reinforcement, like the experimental method, which is complicated, time-consuming, expensive, and laborious. Similarly, existing numerical modeling methods rely on the simplistic geometric representations of the reinforcements, which are insufficient to account for the actual fiber topologies, misalignment, their compaction and nesting effect. The analytical models like Gebart's model [2] and Endruweit's model [3] consider only for various standard fiber placement distribution and arrangement. Another analytical model developed by modifying the constants of Gebart's model for carbon fiber is the Gebart-Endruweit (GE) model [4]. GE model exists only for carbon fiber and is not developed for glass fiber. There is a lack of robust analytical model that can predict the permeability of realistic random arrangement of fibers. These limitations are extensively addressed in the virtual permeability measurement method in which X-ray computed tomography (XCT) combined with computer simulations are used. It is a very effective and flexible technique for characterization of material permeability [5,6]. The permeability of reinforcements can be computed from the XCT images of a single sample, saving time, labor, and cost. The actual fiber topologies, misalignment, compaction, and nesting effects are also considered in this method. Although the virtual permeability method is robust but it is limited by computational power hence permeability is computed for a small sample which could be non-representative. For instance, it was impossible to load the 3D model (detailed in Section 2) used in this study on a desktop with Intel® Xeon® CPU E5-2630B4 @2.20GHz configuration.

In this research, we present a methodology to speed up the computational process of virtual permeability of composite laminates. This method begins by generating the 3D computational model from the stack of XCT images, followed by the division of the model into several smaller domains, named further cells, as consecutive and parallel (CaP) cells. The local permeability of each CaP cell is computed with the commercial computational fluid dynamics (CFD) tool. The obtained permeability values are statistically processed considering individual CaP cell values, resulting in the global permeability. This method was implemented to assess microscale fiber bundle intra-tow permeability during the first International Virtual Permeability Benchmark (IVPB) exercise [7,8]. The method of cells has been successfully used for characterization of mechanical properties of reinforcing textiles [5,9]. The focus of this study is to present the details of the methodology developed during the IVPB exercise by our group. Compared to the conventional method, this method provides an opportunity for faster computation and, most importantly, the possibility to handle samples of size larger than allowed by computational resources, thereby removing the restrictions on the required computer hardware or sample size.

2 MATERIALS AND METHODOLOGY

The XCT image of glass fiber tow was extracted from the X-ray tomographic scan of the twill-weave glass fiber-reinforced composite and provided by the organizer of IVPB exercise. The scans are available on the repository at https://doi.org/10.5281/zenodo.6611926 (fiber diameter: 9 µm, scan volume: 1023*124*973 µm, voxel size: 0.521 µm, ~ 400 fibers in plane, fiber volume fraction: ~ 54-59%) and the details on the image segmentations can be found in Ref. [8].

The segmented XCT images were used to generate the 3D model using in-house developed MATLAB™ script. The generated 3D model was divided into 16 CaP cells, labelled as 11… 44, as shown in Figure 1. Each of the 16 CaP cells was imported to ANSYS™ for generation of finite elements model, followed by mesh generation and fluid flow modeling.

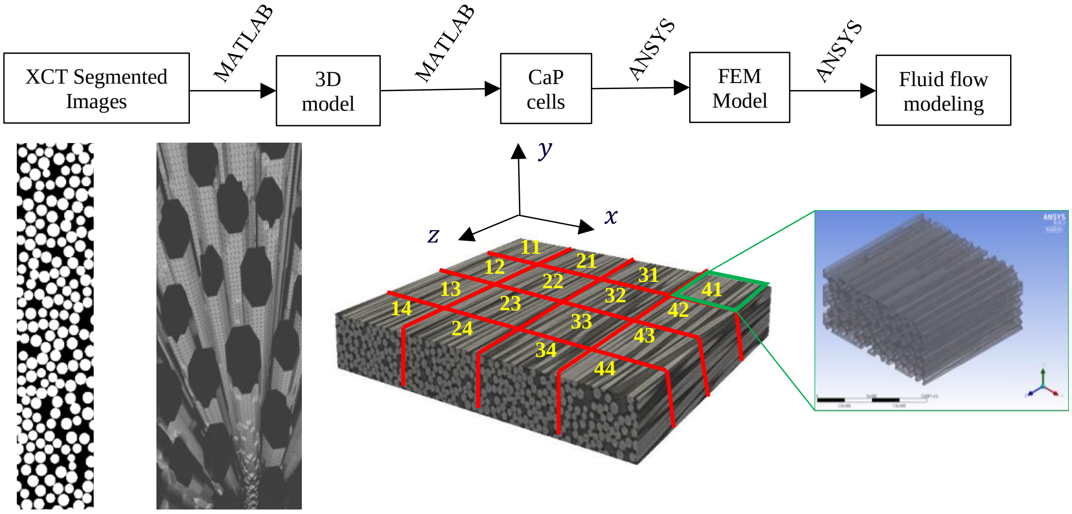

Figure 1. Schematic diagram of 3D model generation, division into CaP cells, and finite element model for fluid flow modeling.

Fluid flow modeling was performed in ANSYS™ CFX to analyze the mass-transport properties and compute permeability for each CaP cell independently. The conservation of mass equation (3) for incompressible fluid and Navier-Strokes equation (4) and were considered for fluid flow simulation as,

$$\nabla u = 0 \tag{3}$$

$$\rho \frac{\partial u}{\partial t} + \rho(u.\nabla)u = -\nabla P + \mu \nabla^2 u + f \tag{4}$$

where u is the velocity $[m/s]$, ρ is the density of fluid $[Kg/m^3]$, f denotes body force $[N]$ (in our case $f = 0$), t is time $[s]$, and P is pressure $[Pa]$.

Two opposite faces of the CaP cell were assigned as inlet and outlet with the applied pressure values. The remaining four faces were assigned as symmetric boundary conditions and a no-slip condition was assigned to the fluid-solid interface. The governing equations (Equations 3, 4) were solved for the fluid domain to obtain the mass flow rate at the outlet with a residual of 10^{-5} as the convergence criterion. The obtained mass flow rate was considered to calculate the permeability of each CaP cell (Equation 2) in three principle directions, providing the local permeability and fiber volume fraction of 16 CaP cells. These permeability values were converted to compute the permeability for the global 3D realistic model as per Equation (5… 10). The schematic of this conversion is shown in Figure 2.

$$K_{xx} = \frac{1}{\left(\frac{1}{K11} + \frac{1}{K21} + \frac{1}{K31} + \frac{1}{K41}\right)} + \cdots + \frac{1}{\left(\frac{1}{K14} + \frac{1}{K24} + \frac{1}{K34} + \frac{1}{K44}\right)} \tag{5}$$

$$K_{zz} = \frac{1}{\left(\frac{1}{K11} + \frac{1}{K12} + \frac{1}{K13} + \frac{1}{K14}\right)} + \cdots + \frac{1}{\left(\frac{1}{K41} + \frac{1}{K42} + \frac{1}{K43} + \frac{1}{K44}\right)} \tag{6}$$

$$K_{yy} = \frac{1}{16}(K11 + K12 + \cdots + K43 + K44) \tag{7}$$

$$K_{xy} = K_{yx} = 0 \tag{8}$$

$$K_{xz} = K_{zx} = 0 \tag{9}$$

$$K_{yz} = K_{yz} = 0 \tag{10}$$

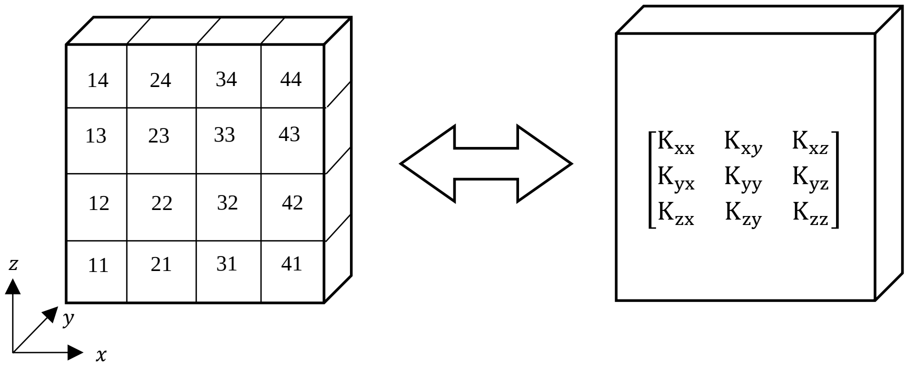

Figure 2. Schematic diagram for converting CaP cells permeability into global permeability

3 RESULTS

The mass flow rates obtained after fluid flow simulation for each of the 16 CaP cells are considered to compute the local permeability. Similarly, the local fiber volume fraction is estimated, considering the volume occupied by the fluid to the total volume of a CaP cell. All 16 local permeability and fiber volume fractions are plotted in Figure 3. The global value of permeability is computed based on these local permeability values and also plotted in Figure 3 for comparison. The global fiber volume fraction is estimated from the global 3D model, considering the volume of fluid to the volume of the global 3D model. Similarly, the permeability of the 3D model was also predicted by the GE model [4] and plotted, as shown in Figure 3, for comparison. It is worth to note that the constants in the GE model [4] are only measured and defined for carbon fiber-reinforced composite but not available for glass fiber-reinforced composite. The constants measured for carbon fiber-reinforced composite are considered here for comparison.

The comparison of the global permeability with the mean values reported in the IVPB exercise for the cluster of the most relevant results and GE model predictions as plotted, as shown in Figure 3, shows a matching trend for permeability calculated along the fiber direction. For the transverse direction, the value calculated by this methodology matches perfectly with the IVPB exercise value; however, the values predicted by the GE model are much lower. The order of values predicted by the GE model matches with the transverse permeability results of this research and the IVPB exercise result, but the constant value differs by as much as 5× for K_{yy} and 2× for K_{xx}.

Figure 3 shows a clear trend of a monotonic decrease in the fiber volume fraction from CaP cell #11 to CaP cell #44, with an abrupt drop when transiting from CaP cell #42 to CaP cell #44. It is also evident from the 3D model demonstrated in Figure 1, where it can be seen that CaP cell #44 has low density of fibers with comparatively higher areas for epoxy, decreasing the overall fiber volume fraction to its lowest value of 46.96% amongst the 16 CaP cells. Evidently, it results in the highest value of permeability for all 3 principle components. In contrast, the highest fiber volume fraction of 60.94% is noted in CaP cell #11 and lowest values of permeability for all 3 principle components are computed for the same CaP cell #11.

The pressure and velocity contour obtained after fluid flow simulation for CaP cell #41, as discussed in Figure 1, is presented in Figure 4 along three principle axes. A pressure of 1 Pascal and 0 Pascal was applied as inlet and outlet boundary condition as evident from pressure contours, as shown in Figure 4a, c and e. The interesting micro-channel flows can be observed in the velocity contours with zero velocity at the solid-fluid interacting location because of no-slip boundary condition. There are several micro-channel flows along the X-axis compared to the ones along the Y-axis and Z-axis, as shown in Figure 4b, d, and f because of comparatively larger gaps along the X-axis of the 3D model. The maximal velocity observed in the micro-channel flow for the pressure difference of 1 Pascal is 1.08 mm/s, 1.18 mm/s, and 4.90 mm/s along X, Y, and Z-axis, respectively, as shown in Figure 4.

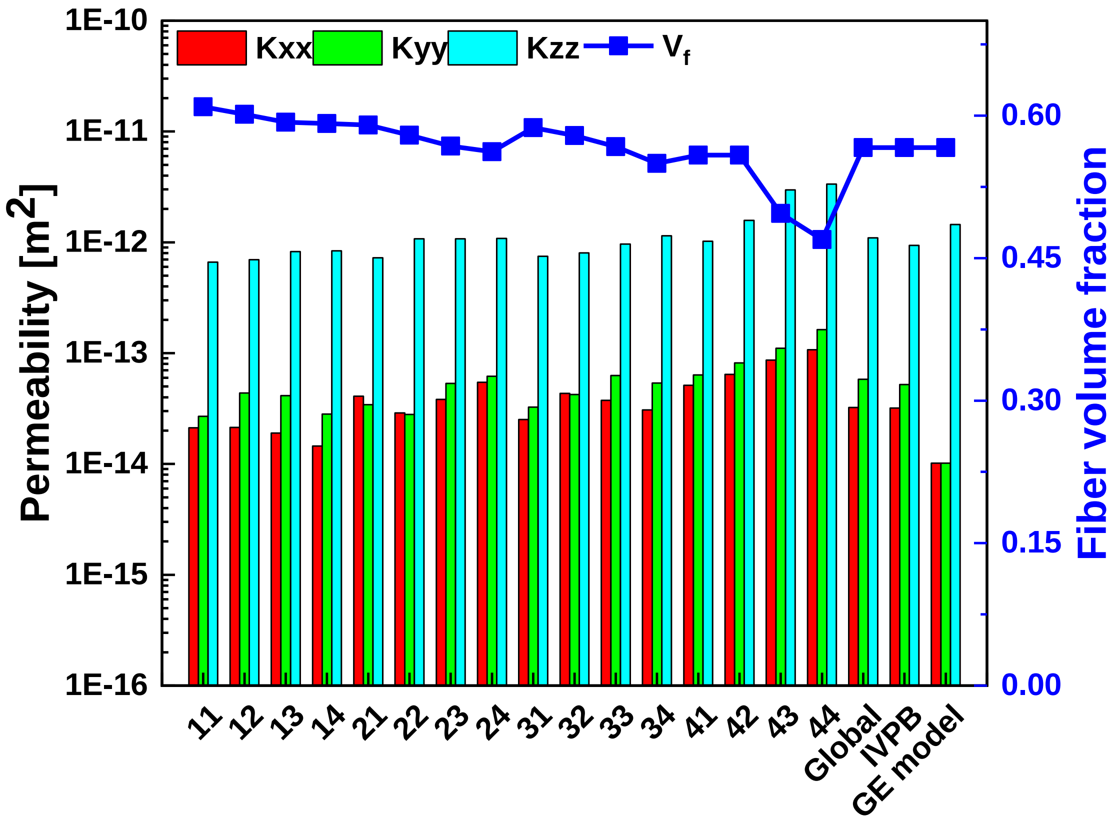

Figure 3. Virtual permeability of different CaP cells (local permeability values) in comparison with permeability of the global model, IVPB exercise and GE model prediction. Variation in fiber volume fraction in local and global model is plotted in secondary axis.

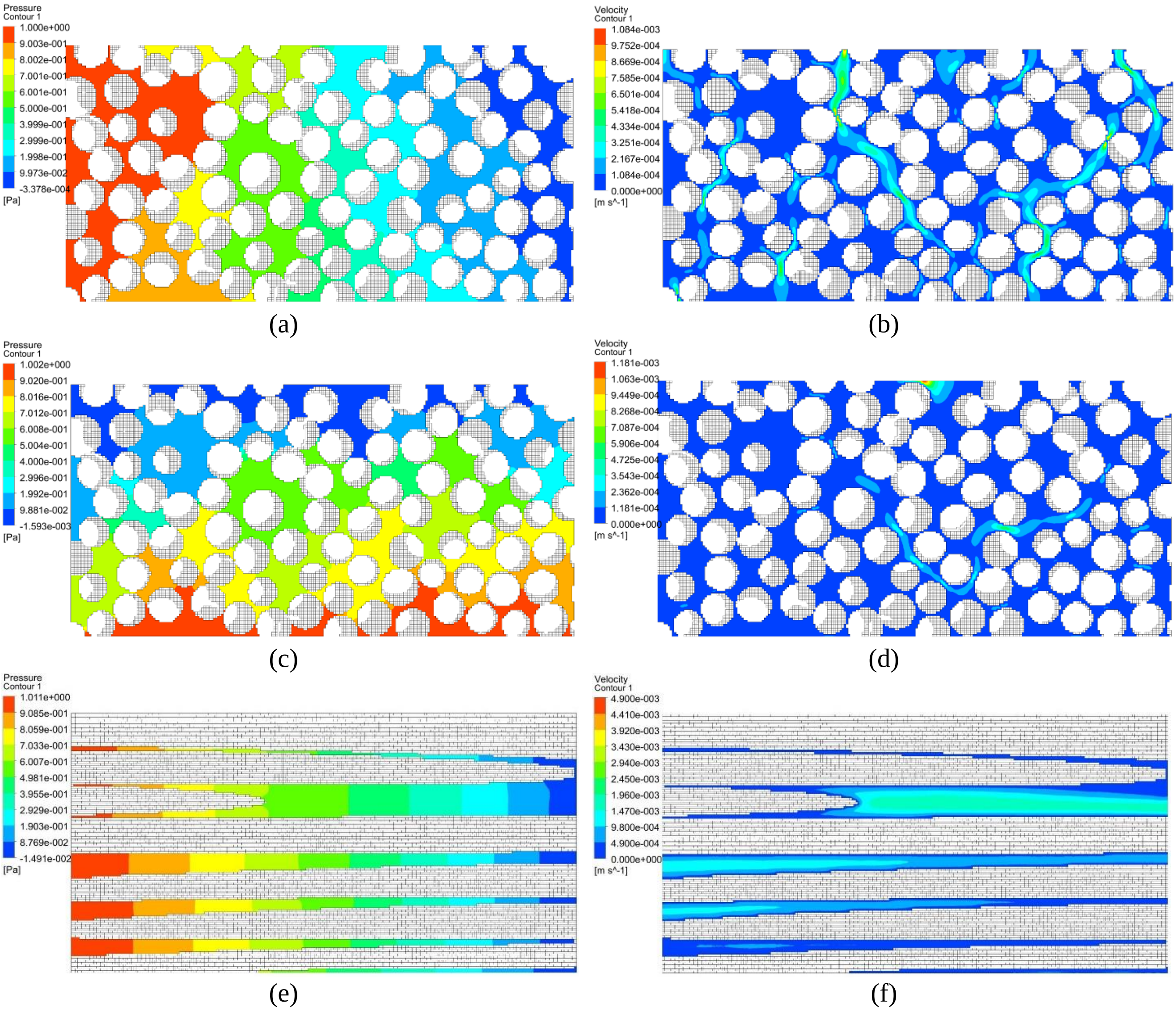

Figure 4. Pressure contour [(a), (c), and (e)] and velocity contour [(b), (d), and (f)] along X, Y and Z axis respectively for CaP cell #41 as shown in Figure 1. Fiber direction is along the Z axis.

4 CONCLUSIONS

The methodology to speed the computation process of virtual permeability of microscale fiber bundle in the composite laminates based on their segmented XCT images is demonstrated. The obtained results are validated by the published literature and analytical predictions, followed by a discussion of errors. Compared to the conventional virtual permeability method, which is limited by the computational resource or size of computational domain, this method provides an opportunity to handle larger sample size than allowed by computational resources, thereby removing the restrictions on the required computer hardware or sample size. Similarly, loading the segmented XCT image data becomes faster, the computation becomes faster as the overall size of the computational domain decreases.

ACKNOWLEDGEMENTS

The authors would like to acknowledge the organizers of the IVPB exercise for inviting for participation in the IVPB exercise. The help of Sergey Mishin and Daniil Padalitsa from Laboratory of Cyber Physical Systems, Skoltech for access to the ANSYS^{TM} system are acknowledged.

REFERENCES

1. Advani, S.G.; Simacek, P. Liquid Composite Molding: Role of Modeling and Simulation in Process Advancement. *ICCM Int. Conf. Compos. Mater.* **2015**, *2015-July*, 19–24.
2. Gebart, B.R. Permeability of Unidirectional Reinforcements for RTM. *J. Compos. Mater.* **1992**, *26*, 1100–1133, doi:10.1177/002199839202600802.
3. Endruweit, A.; Gommer, F.; Long, A.C. Stochastic Analysis of Fibre Volume Fraction and Permeability in Fibre Bundles with Random Filament Arrangement. *Compos. Part A Appl. Sci. Manuf.* **2013**, *49*, 109–118, doi:10.1016/j.compositesa.2013.02.012.
4. Endruweit, A.; Zeng, X.; Long, A.C. Multiscale Modeling of Combined Deterministic and Stochastic Fabric Non-Uniformity for Realistic Resin Injection Simulation. *Adv. Manuf. Polym. Compos. Sci.* **2015**, *1*, 3–15, doi:10.1179/2055035914Y.0000000002.
5. Bodaghi, M.; Vanaerschot, A.; Lomov, S. V.; Correia, N.C. On the Variability of Mesoscale Permeability of a 2/2 Twill Carbon Fabric Induced by Variability of the Internal Geometry. *Compos. Part A Appl. Sci. Manuf.* **2017**, *101*, 394–407, doi:10.1016/j.compositesa.2017.05.030.
6. Ali, M.A.; Umer, R.; Khan, K.A.; Cantwell, W.J. Application of X-Ray Computed Tomography for the Virtual Permeability Prediction of Fiber Reinforcements for Liquid Composite Molding Processes: A Review. *Compos. Sci. Technol.* **2019**, *184*, 107828, doi:10.1016/j.compscitech.2019.107828.
7. May, D.; Syerko, E.; Schmidt, T.; Binetruy, C.; Silva, L.R. da; Lomov, S.; Advani, S. Benchmarking Virtual Permeability Predictions of Real Fibrous Microstructure. In Proceedings of the American Society for Composites 2021; Destech Publications, Inc., September 20 2021.
8. Syerko, E.; Schmidt, T.; May, D.; Binetruy, C.; Advani, S.G.; Lomov, S.; Silva, L.; Abaimov, S.; Aissa, N.; Akhatov, I.; et al. Benchmark Exercise on Image-Based Permeability Determination of Engineering Textiles: Microscale Predictions. *Compos. Part A Appl. Sci. Manuf.* **2023**, *167*, 107397, doi:10.1016/j.compositesa.2022.107397.
9. Prodromou, A.G.; Lomov, S. V.; Verpoest, I. The Method of Cells and the Mechanical Properties of Textile Composites. *Compos. Struct.* **2011**, *93*, 1290–1299, doi:10.1016/j.compstruct.2010.09.022.